4 Flow over a Vertical Flat Plate

Free convection boundary layer over a vertical flat plate has been widely studied because of its various scientific and real-life applications. Although the analytical solution of the velocity boundary layer thickness is well-known, its experimental validation is presently limited. This chapter presents the visualization and measurement of a laminar FCBL formed over a heated vertical flat plate by PIV technique. A detailed description of PIV challenges and measures to overcome these challenges when measurements are taken near a solid wall has also been provided. The analytical solution for a 2-D steady, laminar FCBL equations at a value of Prandtl number obtained at experimental conditions and a comparison of the experimental results with this analytical solution is also reported in this chapter.

4.1 Theoretical background

A steady, laminar, 2-D and incompressible FCBL formed over a vertical flat plate is shown in figure 4.1. The FCBL equations assuming Boussineq approximation is well known [4,20,71]. Using similarity analysis, Sparrow et al. (1956) obtained the non-dimensional form of boundary layer equations as

$$f''' - 3(f')^2 + 4ff'' + \theta = 0 \tag{4.1}$$

$$\theta'' + \mathrm{Pr}(4f\theta' - \theta f') = 0 \tag{4.2}$$

subject to the boundary conditions:

$$f(0) = f'(0) = 0, \theta'(0) = -1 \tag{4.3}$$

$$f'(\infty) = 0, \theta'(\infty) = 0 \tag{4.4}$$

The local Nusselt number is given by

$$Nu_x = \frac{1}{\theta(0)}\left(\frac{Gr_x^*}{5}\right)^{1/5} \tag{4.5}$$

where Gr_x^* is the local modified Grashof number which is defined as $Gr_x^* = \frac{g\beta q_w'' x^4}{\vartheta^2 k}$

The wall shear stress is defined as

$$\tau_w = \mu \frac{\partial u}{\partial y}\Big|_{y=0} = \frac{5\mu\vartheta}{x^2}\left(\frac{Gr_x^*}{5}\right)^{3/5} f"(0) \tag{4.6}$$

The wall skin friction coefficient is defined as

$$c_{fx} = \frac{\tau_w}{\frac{1}{2}\rho u_{ref}^2} = \frac{2}{5}\left(\frac{Gr_x^*}{5}\right)^{-1/5} f"(0) \tag{4.7}$$

where
$$u_{ref} = 5\left(\frac{Gr_x^*}{5}\right)^{2/5}\frac{\vartheta}{x} \tag{4.8}$$

Equations (4.1) - (4.2) are coupled ordinary non-linear differential equation. These equations with the boundary conditions given by equation (4.3) and (4.4) were solved by a shooting method [21]. For solving these equations, the mathematical condition $\eta \to \infty$ must be replaced by a large finite number (η_{max}) which ensures that the flow parameters asymptotically approach to their final values [72]. The value of η_{max} has been chosen as 20 after preliminary investigation of the effect of different values of η_{max} on the values of $f''(0)$ and $\theta(0)$. Here, $f''(0)$ and $\theta(0)$ are important quantities for the determination of shear stress and Nusselt number respectively as seen from equations (4.5) - (4.6). Table 4.1 shows the values of $f''(0)$ and $\theta(0)$ for different η_{max} at a Prandtl number *(Pr)* of 6.14 (for water at 25 °C). As seen from table 4.1, the values of $f''(0)$ and $\theta(0)$ do not change upto six decimal places for $\eta_{max} \geq 20$.

Table 4.1: Analytical non-dimensional velocity and temperature gradients at the wall for different values of η_{max} and *Pr* = 6.14

$\boldsymbol{\eta_{max}}$	**5**	**10**	**20**	**40**	**50**
$\boldsymbol{f''(0)}$	0.368083	0.368213	0.368215	0.368215	0.368215
$\boldsymbol{\theta(0)}$	0.859706	0.859058	0.859051	0.859051	0.859051

Figure 4.2 shows the velocity profile obtained from similarity analysis for Pr = 6.14. The similarity solution gives an asymptotic nature of the velocity profile. Hence, the edge of the boundary layer in free convection cannot be defined like is done in case of forced convection i.e. as a fraction of the bulk fluid velocity (Goodrich et al., 2019). The edge of the free convection velocity boundary layer can be defined using a threshold value of *u-velocity* (Goodrich, 2017; Baudoin et al., 2017). The threshold value adopted in the present work is based on the maximum velocity (u_{max}) in the velocity profile and its value is equal to $0.01u_{max}$ in the boundary layer. Therefore, in figure 4.2, the edge of the boundary layer is marked at the location where $f' = 0.01f'_{max}$ and the non-dimensional velocity boundary layer thickness ($\bar{\delta}$) is equal to 6.58 for $Pr = 6.14$. The overall velocity boundary layer is a combination of two regions: an inner layer in which the velocity rises from zero to a maximum value ($f'_{max} = 0.103675$ at $\eta = 0.71$) and an outer layer in which the velocity asymptotically approaches to zero from its maximum value.

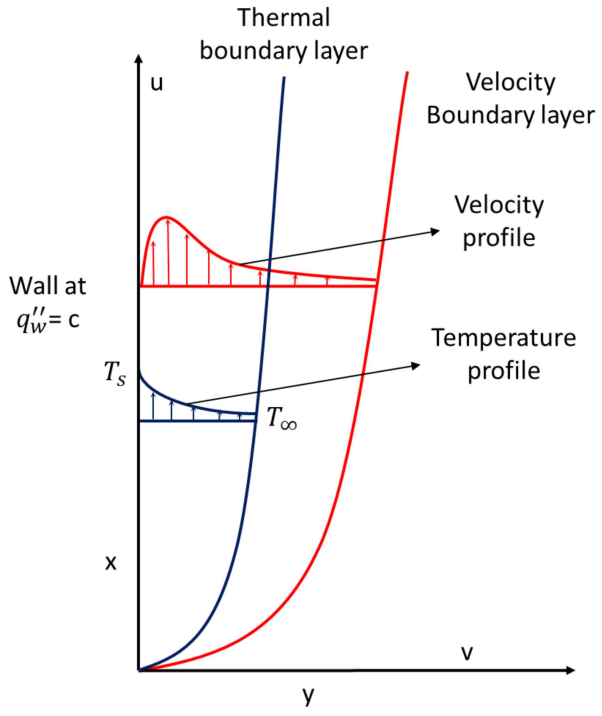

Figure 4.1: Free convection velocity and thermal boundary layers for $Pr > 1$

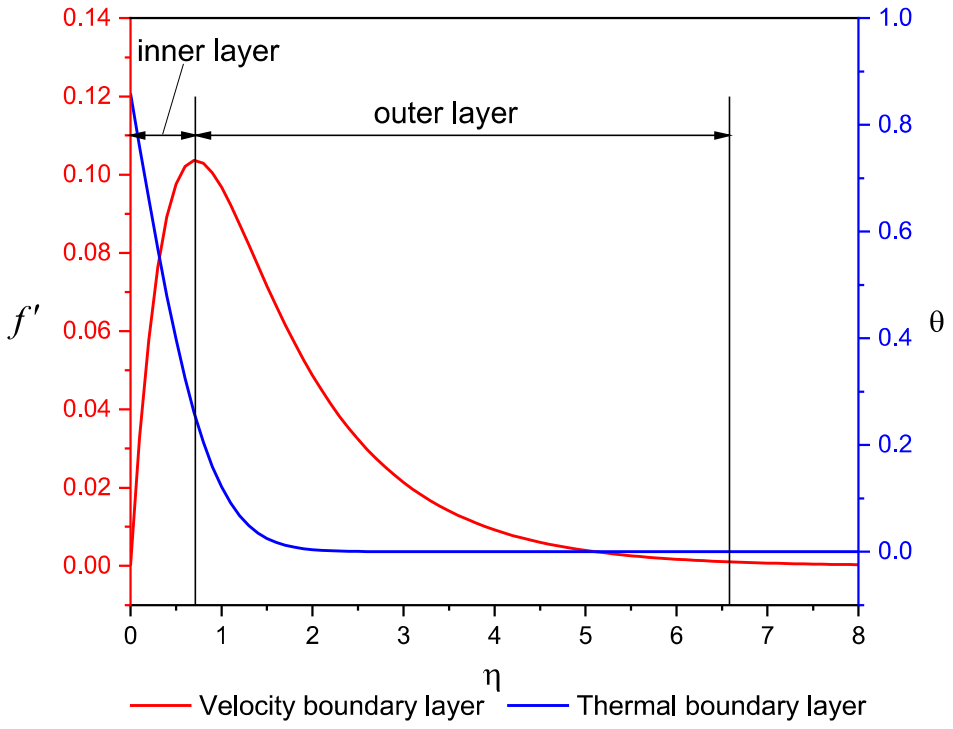

Figure 4.2: Analytical solution of free convection boundary layer at Pr = 6.14

4.2 Experimental Details

4.2.1 Free convection setup

In this work, a vertically-placed copper plate of length 150 mm, width 100 mm and thickness 0.5 mm was used as a heating surface. A silicone rubber heater was used for heating the plate. The plate was attached to the heater with pressure sensitive adhesive in such a way that there is no air gap between plate and heater. A 25 mm thick Teflon insulation is provided on the back side of the heater as shown in figure 4.3. Since copper has a thermal conductivity of about 385 W/m.K, this works out to be about 1540 times higher than that of Teflon. Assuming one-dimensional heat conduction, the thermal resistance provide by Teflon is 77,000 times higher than copper. Also, the fraction of area of the edges of the plate to the front surface area (which is in contact with water) is only 1.6%. To further ensure one dimensional heat transfer, the edges of the plate are also insulated. Therefore, heat loss by conduction through the insulation was negligible. A

variable electric power is provided to the heater by a dimmerstat. The plate was kept in a glass tank having dimensions of 600 (x) × 600 (y) × 500 (z) mm. It is possible that if the free surface and tank walls are sufficiently close to the plate, fluid circulation and stratification may be produced, which would adversely affect the experimental results. To rule out the presence of these effects, the plate was placed at a sufficient distance from the free surface and tank walls. This distance was optimized after performing many trial runs in which the velocity field near the free surface and tank walls was measured till negligible values were obtained. Based on these considerations, the plate was placed 300 mm below the free surface of the water and leading edge of the plate was 100 mm above the bottom wall of the tank as shown in figure 4.3.

The surface temperature of the plate was measured by five sheathed T-type thermocouples having a diameter of 0.5 mm. All the thermocouples were calibrated using a thermostatic bath and a four wire master RTD having an accuracy of 1/10 DIN. The thermocouples were embedded through the back side of the plate-heater assembly and the tip of the thermocouples was exactly aligned with the front surface of the plate as shown in figure 4.3. With this arrangement, it has been ensured that the thermocouples measure the surface temperature accurately and also, not disturb the flow over the wall. The mean readings of three other thermocouples (one at the top, second at the centre and the third at the bottom of the tank) were used to calculate the bulk temperature of water. All the thermocouples readings were recorded by a data acquisition system. The experiment was done with a bulk water temperature of 25 $\pm$ 0.1 ℃ in a room which was also maintained at a temperature of 25 ℃. The top surface of the tank was kept covered by a 10 mm thick acrylic sheet to reduce the effect of random air flow over the free surface.

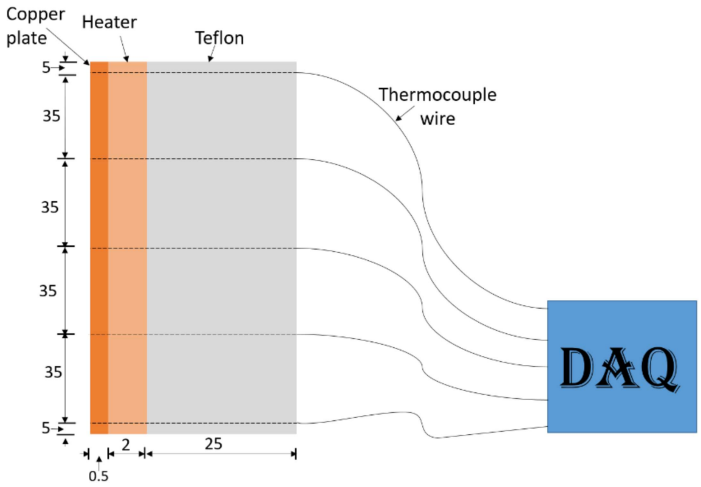

All dimensions are in mm

Figure 4.3(a): Schematic diagram of copper plate, thermocouples and insulation assembly

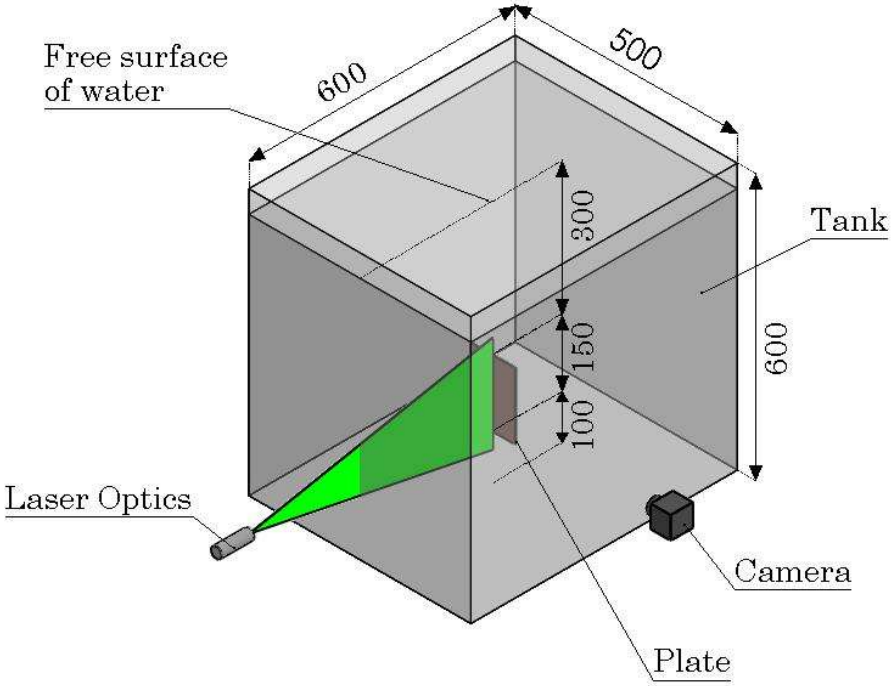

All dimensions are in mm

Figure 4.3(b): Schematic diagram of experimental setup with position of the camera, laser sheet and copper plate

4.2.2 PIV technique for velocity measurement

Although PIV is a widely used technique for velocity measurement, near-wall measurement by this technique poses the following challenges [67,74,75]:

1. The selection of suitable seeding particles
2. Wall reflection
3. Biased velocity estimates
4. The analysis of particle image displacement

The selection of suitable seeding particles is needed to accurately follow the fluid flow. Hollow glass spheres made of borosilicate and having a mean diameter of 10 μm, density 1.1 g/cm^3 and refractive index 1.52 were used in this work as seeding particles. The particle Stokes number, which is a measure of a particle's followability was calculated to be less than 0.1. Hence, the seeding particles would follow the flow with fidelity [66]. The gravitational induced velocity or settling velocity of seeding particle was calculated from the Stokes drag law to be equal to 6.13 μm/sec, which is much lower compared to the velocity range to be measured. A particle image density of 5 - 10 is needed in an interrogation window for better correlation coefficient [66,76]. Based on this consideration, 2.5 g of seeding particles were added to the glass tank containing double distilled water. The seeding particles were mixed uniformly by stirring and the experiment was started after 10 hours of mixing of seeding particles. This ensures that all particles are uniformly mixed and bulk fluid velocity, if any, created by stirring has become negligible.

The wall reflection is the most important cause of discrepancy in velocity measurement by PIV close to the wall. When a laser light is incident on the surface of a plate, reflection from the surface produces a high intensity region near the plate surface which affects the correlation between two images. For reducing this surface reflection, the front surface of the plate was spray-painted with matt black [77,78]. Also, the background

elimination method which is discussed later in this section, has been used in the pre-processing steps of image processing to reduce the reflection from the wall.

The velocity measured by PIV is biased when particle images are much smaller than the size of a pixel. This phenomenon is called "pixel locking", in which the displacement information tends to be biased towards discrete pixel values [66]. Particle image diameter is an important parameter for the assessment of PIV performance [66,76] and is calculated as:

$$d_{image} = \left[\left(Md_p\right)^2 + (2.44(1+M)f_{\#}\lambda)^2\right]^{\frac{1}{2}} \tag{4.9}$$

The particle image diameter from equation (4.9) is calculated as 3.083 pixel in this work, which is greater than the 2 pixels. This ensures that there is no pixel locking effect [66]. However, measured velocity may still be biased due to a large velocity gradient and image processing methods used to estimate the particle image displacement.

In free convection, low velocities are encountered. As a consequence, the images were acquired in a single frame mode [79] with a frequency of 15 Hz i.e., time between pulses is 66.67 ms. In the present work, as the flow is laminar and steady, it is appropriate to estimate the time averaged velocity field. The number of images acquired were 1000, which is sufficient to accurately determine the time averaged velocity field. The wall was identified carefully based on the intensity statistics. The acquired images contain background noise (reflection from tank walls and plate surface) which was minimised by using the background elimination technique. In this technique, the mean of all images is subtracted from the parent or raw images [74,80]. The images before and after the background elimination respectively are shown in figure 4.4(a) and 4.4(b). These figures clearly demonstrate that background noise is reduced after applying the background elimination technique. As the region of interest is small, an image masking technique has

been applied to remove the area of no interest. Figure 4.5 shows PIV image after masking with two conditions: - (1) half of the interrogation area inside the wall (IA1) and (2) interrogation area aligned with the wall (IA2). The particle image displacements with IA1 and IA2 conditions near the wall were analysed using both ensemble correlation and adaptive correlations. The algorithms used to obtain average velocity vectors in these correlations are already described in chapter 3. In the ensemble correlation method, the correlation function of each interrogation area is averaged at each position for all the images. Therefore, ensemble correlation gives the average or mean velocity flow field [66,81]. A fixed interrogation area of size 16 pixels × 16 pixels and an overlap of 50% is used for ensemble correlation. In adaptive correlation, interrogation area size, shape and location are iteratively adjusted based on the particle image pairs between maximum and minimum interrogation area size. The minimum and maximum interrogation area size 16 pixels × 16 pixels and 64 pixels × 64 pixels respectively with a grid step size of 8 pixels × 8 pixels have been used for this correlation. The time-averaged velocity field has been calculated by averaging all the instantaneous velocity fields obtained from the adaptive correlation. The number of vectors in the camera's field of view (155 mm × 155 mm) is 65,025, which means that the distance between two adjacent vectors is 0.60 mm.

A comparison of velocity profiles obtained with adaptive and ensemble correlation at x = 75 mm, and at heat fluxes of 500 W/m^2 and 1500 W/m^2 is shown in figure 4.6. Figure 4.6 also shows the comparison of two PIV image masking conditions (IA1 and IA2). For the case of IA1 condition (figure 4.6(a) and 4.6(b)), as half of the interrogation area is inside the wall, the first velocity vector was obtained at the wall. For the case of IA2 (figure 4.6(c) and 4.6(d)), the closest velocity vector from the wall was obtained 0.60 mm away from the wall since the interrogation area is aligned with the wall. The velocity data was extrapolated up to the wall by assuming a no-slip condition (zero velocity) at the wall. It can be clearly

seen from figure 4.6 that both the correlations with IA1 and IA2 conditions closely match with the analytical solution in the outer layer of the boundary layer. For the case of IA1, both the adaptive as well as ensemble correlation are biased towards higher displacements at the wall, signifying a non-zero finite velocity at the wall as shown in figures 4.6(a) and 4.6(b). This is due to the fact that one half of the interrogation area is inside the wall and other half is seeded with the particles. Therefore, the obtained particle image displacement is associated only with the seeded part of the IA1 [67,82]. Also, due to the iterative interrogation window deformation method used in adaptive correlation, it shows higher particle displacement compared to ensemble correlation near the wall. The velocity vectors obtained from ensemble correlation, wherein the wall is aligned with the interrogation area (IA2) were more accurate compared to adaptive correlation and this is shown in figures 4.6(c) and 4.6(d). The reason for this is that the use of ensemble correlation enhances the signal to noise ratio and dynamic velocity range and reduces the effect of low seeding density close to the wall [66,68,81]. Raffel et al. (2018) have also shown that the correlation averaging provides better results than vector averaging. Therefore, in the present work, ensemble correlation with IA2 condition has been used.

In the present work, the temperature difference between the plate surface and fluid is at most 15 °C, resulting in a minimal change in the refractive index. For instance, at a wavelength of 546.1 nm, the refractive index of water only changes from 1.334 to 1.332 with a temperature variation of 20 °C to 37 °C. Thus, a 17 °C temperature change would result in a refractive index change of only 0.15% [83]. Therefore, in the present work, the effect of the refractive index variation on PIV measurements is neglected.

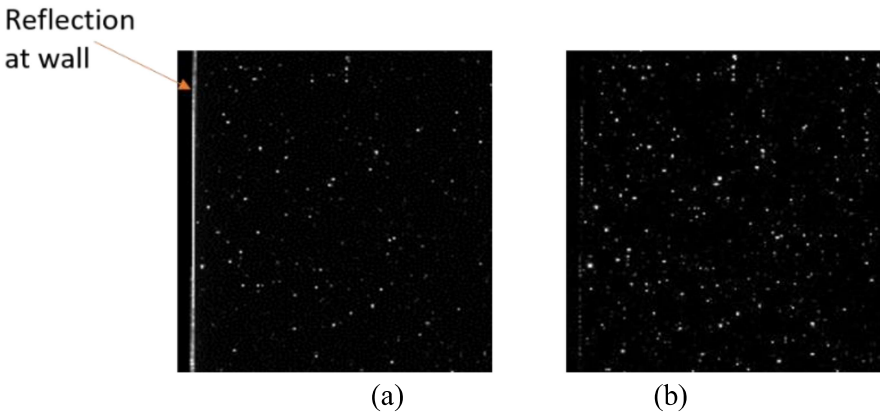

Figure 4.4: Background elimination technique (a) acquired raw image and (b) image after background elimination

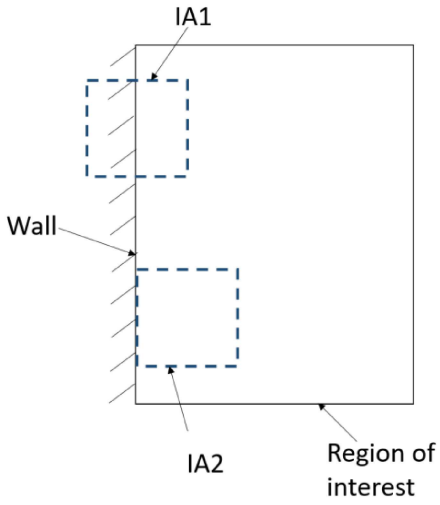

Figure 4.5: Masking PIV raw image with interrogation area inside the wall (IA1) and aligned with the wall (IA2)

Case 1: IA1 Condition

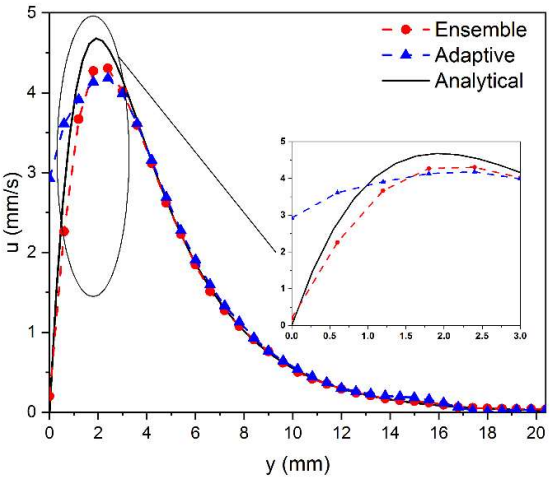

(a) 500 W/m^2

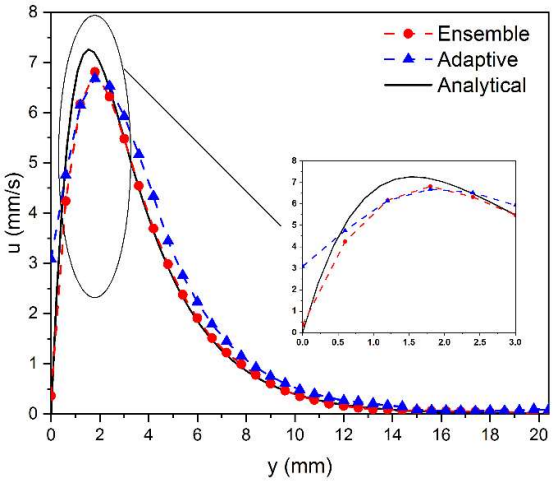

(b) 1500 W/m^2

Case 2: IA2 Condition

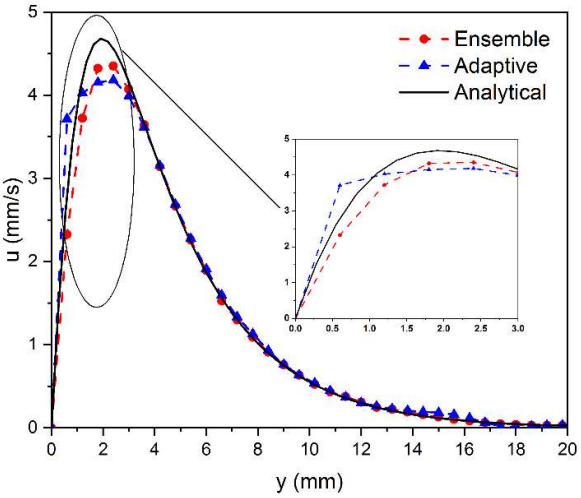

(c) 500 W/m^2

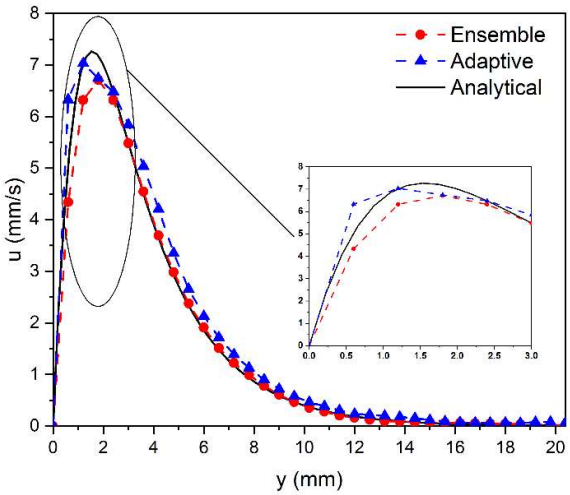

(d) 1500 W/m^2

Figure 4.6: Comparison of adaptive and ensemble correlation algorithm with IA1 condition and at heat flux of (a) 500 W/m^2 (b) 1500 W/m^2; (c) – (d) at same heat fluxes with IA2 condition

4.3 Results and Discussion

The objective of the present investigation was to get a complete description of the velocity boundary layer using PIV. In this section, the experimental results for velocity boundary layer, streamlines, wall shear stress and Nusselt number are presented. The experiments were performed with three different constant wall heat fluxes of 500, 800 and 1500 W/m^2 at steady and laminar conditions. The maximum Gr_L^* based on the plate length and fluid properties at bulk fluid temperature has been estimated to be 3.79×10^9. In previous studies, it has been shown that the fluid flow over a vertical flat plate is in the laminar region when Gr_L^* is less than 10^{13} (Bejan, 2013; Holman, 2010). Hence, in the present work, the flow is in a laminar regime. The results are presented at the mid plane of the vertical plate. These results are also compared with the analytical solution.

4.3.1 Temperature measurement

In free convection, the velocity and temperature field are interdependent i.e. it is a coupled phenomenon. Therefore, the velocity boundary layer characteristics depends on both the plate and bulk fluid temperature. As per the objective of the study, experiments have been performed in a steady state condition which implies that the temperature of the plate and fluid remains constant with time. The temperature difference between the plate surface and the bulk fluid as a function of time at different heat fluxes is depicted in figure 4.7. For clarity, the readings of only two thermocouples located at x = 75 mm and x = 145 mm are shown. The heating of the plate was started after maintaining the bulk fluid temperature at 25 °C with an accuracy of ± 0.1 °C. As shown in figure 4.7, the temperature first increases and reaches a nearly constant value after some time. This ensured that steady state conditions were attained i.e. the heat transfer due to conduction by plate was equal to heat taken away due to convection. It was also observed that with an increase of heat flux, the time taken to reach the steady state condition decreased. This is due to the fact that with

an increase of heat flux, the rate of heat transfer at the wall also increases. The maximum time taken to reach steady state was about 10 minutes for a heat flux of 500 W/m^2. The steady state temperature increases along the surface of the plate and it was found that the maximum temperature is obtained near the trailing edge of the plate at a particular heat flux.

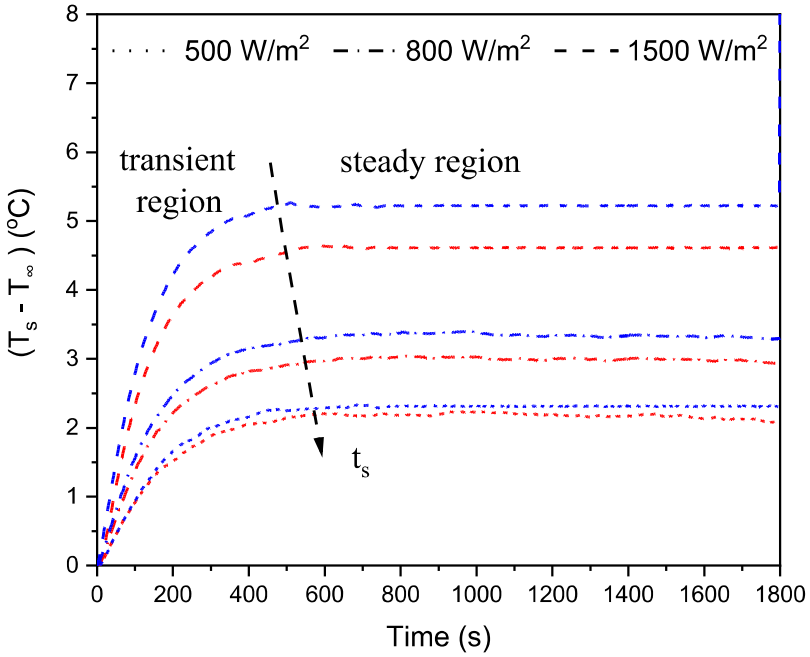

Figure 4.7: Variation of surface temperature with time at x = 75 mm (red colour) and x = 145 mm (blue colour) and heat fluxes of 500, 800 and 1500 W/m^2

4.3.2 Velocity contours and streamlines

The complete description of the boundary layer was successfully obtained after post processing of acquired images as discussed earlier. Figures 4.8 shows the velocity contour and streamlines at a heat flux of 500 W/m^2. The velocity contour gives the magnitude of the velocity vector and streamlines provide the direction of the flow. It is observed from figure 4.8 that the fluid is accelerating over the plate due to heating of the plate. The plate transfers heat to the surrounding fluid and as a result, the density of the fluid close to the wall decreases. The density difference between the bulk fluid and the fluid close to the wall

causes a buoyancy force within the fluid. Owing to this buoyancy force, the movement of fluid takes place over the plate. As the heated fluid (of lower density) close to the wall moves upward, the entrainment of fluid takes place from the bulk fluid (higher density) region. The streamlines, which are depicted in figure 4.8(b), show the entrainment of water in the boundary layer taking place from the transverse direction. These streamlines are similar in pattern to the streamlines obtained from analytical solution by Guha et al. (2017) and Armfield et al. (2007). It is also observed from figure 4.8 that the width of the boundary layer increases along the plate due to momentum diffusion. The maximum velocity and boundary layer thickness occurs near the trailing edge of the plate. A similar shape of the profile of velocity boundary layer was visualized for other heat fluxes and is not shown here due to similarity in pattern.

4.3.3 Velocity profiles

In the present work, the temperature difference between bulk fluid and plate is very small and hence the variation in properties of fluid with temperature is assumed negligible. Therefore, the properties of fluid are taken as constant at a bulk fluid temperature of 25 °C. Due to the constant properties of fluid, the modified Grashof number depends only on the heat flux and location along the plate. Hence, variation of velocity boundary layer with different streamwise locations and heat fluxes are presented. Figure 4.9(a) shows the u-velocity and temperature profiles at different streamwise locations along the plate at a heat flux of 500 W/m^2 and figure 4.9(b) shows the u-velocity and temperature profiles at three different heat fluxes at x = 75 mm. The results near the leading and the trailing edge of the plate are not shown. It is observed from figure 4.9 that the u-velocity increases from zero (no-slip condition at the wall) to a maximum and then asymptotically approaches the zero velocity of the bulk fluid. The thickness of inner layer is very small compared to the outer

layer in all cases, resulting in a sharp rise of velocity from zero to a maximum. This indicates that large velocity gradients exist at the wall.

(a)

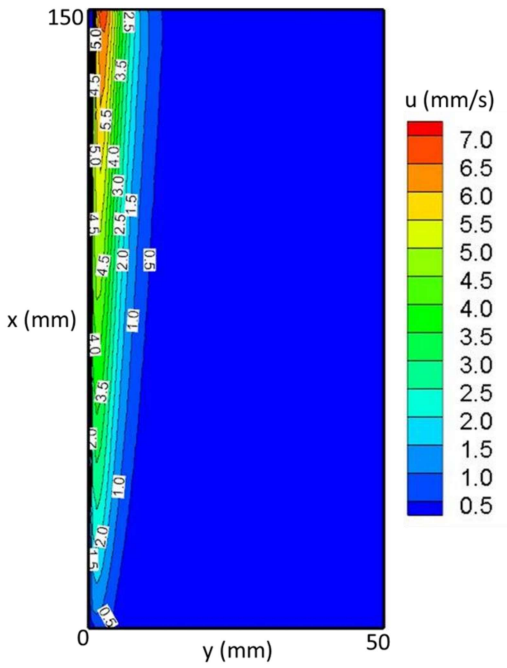

(b)

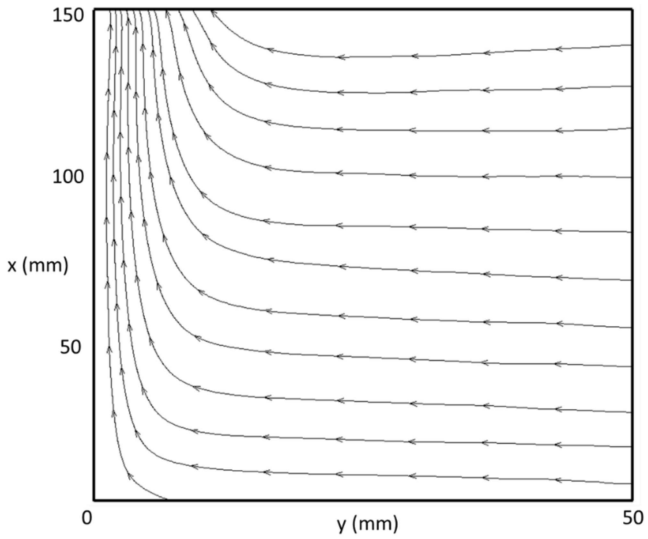

Figure 4.8: (a) u-velocity contour and (b) streamlines obtained from PIV experiment at a heat flux of 500 W/m^2

The inner layer thickness increases i.e. the peak of the velocity profile is shifted away from the wall with the streamwise distance from the leading edge as shown in figures 4.9(a) and 4.10(a). Also, the maximum velocity increase with the streamwise distance from the leading edge, as shown in figure 4.9(a). However, in figure 4.9(a), it is important to note that although inner layer thickness increases, the velocity gradient also increases along the plate. This is due to the fact that increase in u_{max} is more compared to increase in inner layer thickness. For example, the value of inner layer thickness and u_{max} for 500 W/m^2 at x = 50 mm are 2.01 mm and 3.48 mm/s respectively and for 500 W/m^2 and x = 100 mm, these values are 2.24 and 5.22 mm/s respectively as shown in figures 4.9(a) and 4.10(a). So, there is an increase of 11.44% in inner layer thickness compare to a 50% increase in u_{max}. Figure 4.9(b) and 4.10(a) show that the inner layer thickness decreases with heat flux i.e. the peak of the velocity profile shifts towards left but figure 4.9(b) also shows that the maximum velocity increases with the increase of heat flux. For example, the inner layer thickness and u_{max} for 500 W/m^2 at x = 75 mm are 2.17 mm and 4.39 mm/s respectively and for 1500 W/m^2 at x = 75 mm, these values are 1.72 mm and 6.72 mm/s respectively as shown in figures 4.9(b) and 4.10(a). Therefore, the slope of the velocity profile or velocity gradient at the wall increases with an increase in heat flux (due to increase of u_{max} and decrease of inner layer thickness with the heat flux) as seen in figure 4.9(b). The variation of overall boundary layer thickness i.e. summation of inner and outer boundary layer thickness with the locations along the plate and at different heat fluxes, is shown in figure 4.10(b). Since the velocity near the edge of the boundary layer asymptotically approaches the quiescent velocity, large variation in the value of boundary layer thickness can occur based on choice of the parameter to define the boundary layer edge. The identification of the edge of the boundary layer thickness has been described in section 4.2. As seen from figure 4.10(b), the boundary layer thickness increases with location along the plate and

(a)

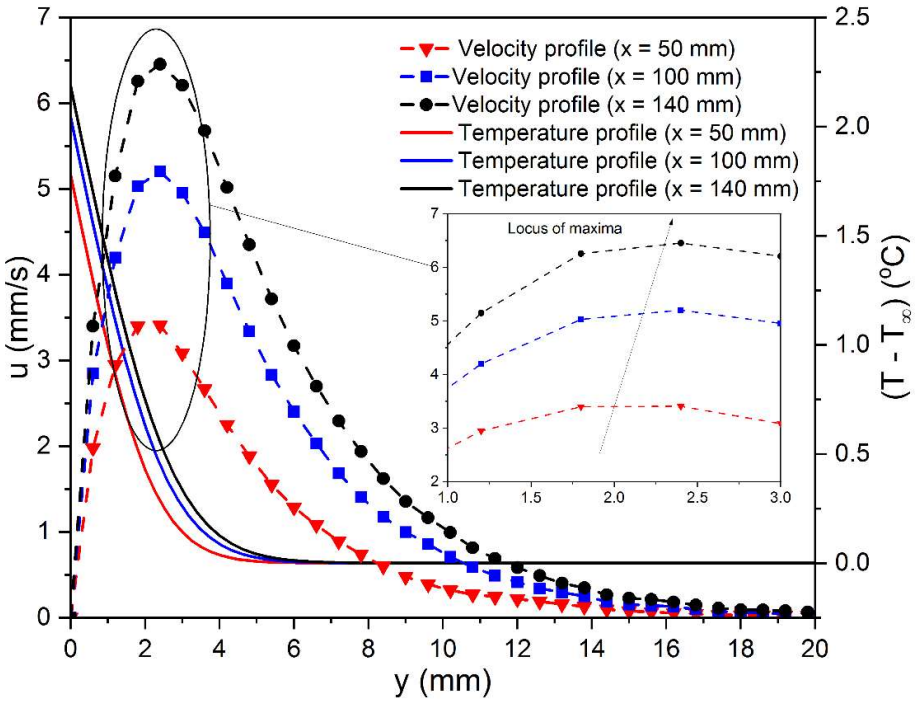

(b)

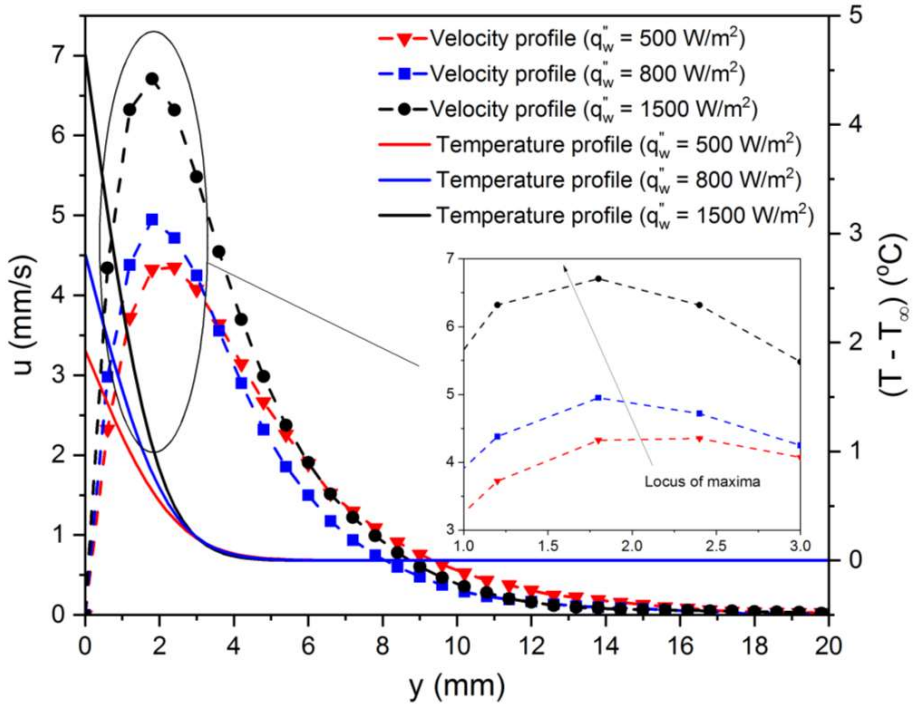

Figure 4.9: Experiemnal u-velocity (dash lines) and analytical temperature (solid lines) profiles (a) for different streamwise locations at 500 W/m^2 (b) for different heat fluxes at x = 75 mm

decreases with the heat flux, similar to the inner layer thickness. The maximum boundary layer thickness occurs at q''_w = 500 W/m^2 and x = 140 mm where its value is 19.79 mm. From figure 4.10, it can be also seen that the overall boundary layer consists of a thin inner layer (~ 2 mm) and a thicker outer layer (~ 15 mm).

(a)

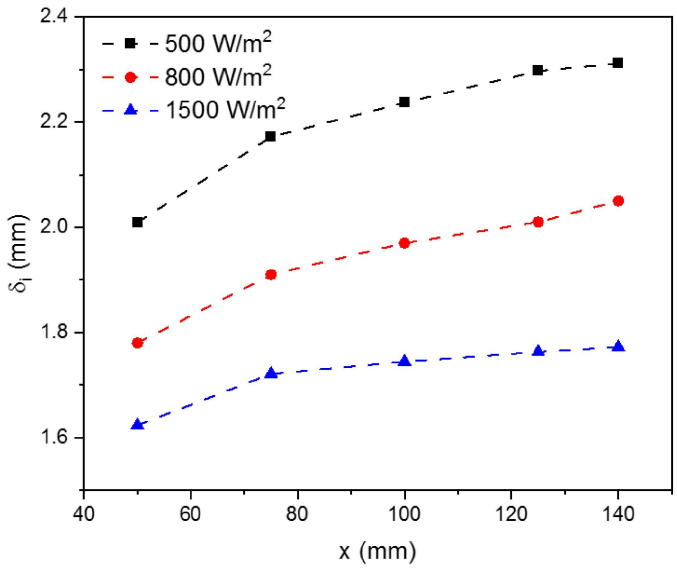

(b)

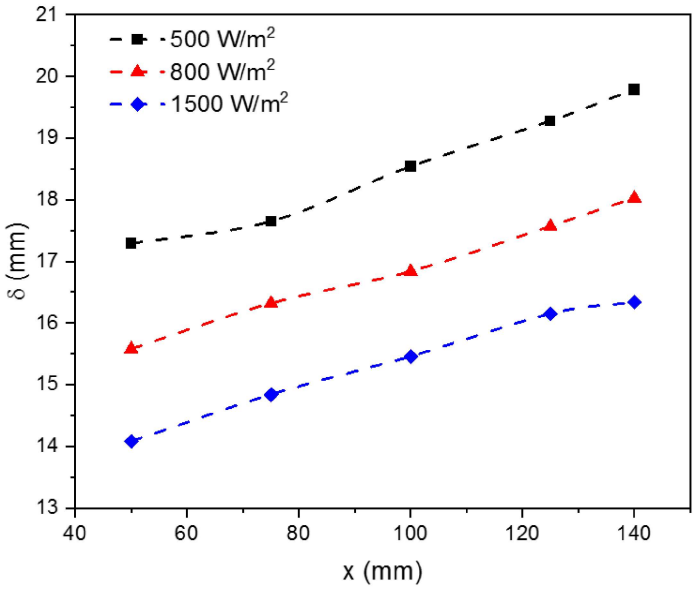

Figure 4.10: Variation of (a) inner and (b) overall boundary layer thickness with location along the plate obtained from PIV experiment at heat fluxes of 500, 800 and 1500 W/m^2

4.3.4 Comparison of experimental and analytical results

As the surface temperature is measured at 5 different locations (x = 5, 40, 75, 110 and 145 mm) along the plate and at three different heat fluxes (500, 800 and 1500 W/m^2), these temperatures have been used to calculate local Nusselt number.

$$Nu_x = \frac{q''_w x}{k(T_s - T_\infty)_x} \tag{4.10}$$

where $(T_s - T_\infty)_x$ is the difference in the surface and bulk fluid temperature at any location along the plate x. The local Nusselt number is plotted against local modified Grashof number and compared with the equation 4.5 of the analytical solution. The results are shown in figure 4.11(a). It is clearly seen that the local Nusselt number increases with the modified Grashof number and its maximum experimental value of 68.12 occurs at x = 145 mm and 1500 W/m^2. From the analytical solution, the parameter $\frac{Nu_x}{(Gr_x^*)^{1/5}} = 0.84$ is obtained for a the *Pr* = 6.14. The experimental data points give the mean value of this parameter as 0.85 with a standard deviation of 0.05 indicating that experimental and analytical Nusselt number are in close agreement. Using the propagation-of-error analysis [85], the maximum uncertainty in the estimation of the Nusselt number for measurements can be determined as follows:

$$\frac{\delta(Nu)}{Nu} = \sqrt{\left(\frac{\delta q''_w}{q''_w}\right)^2 + \left(\frac{\delta \Delta T}{\Delta T}\right)^2} \tag{4.11}$$

For the estimation of heat flux following relation has been used:

$$q''_w = \frac{q_w}{A} = \frac{VI}{A} \tag{4.12}$$

The uncertainty in the estimation of heat flux is determined by the measurement uncertainties associated with voltage (V), and current (I), which were measured during our experiments and is given by

$$\frac{\delta q_w''}{q_w''} = \sqrt{\left(\frac{\delta V}{V}\right)^2 + \left(\frac{\delta I}{I}\right)^2} \tag{4.13}$$

Therefore, equation (4.11) can be written as

$$\frac{\delta(Nu)}{Nu} = \sqrt{\left(\frac{\delta V}{V}\right)^2 + \left(\frac{\delta I}{I}\right)^2 + \left(\frac{\delta \Delta T}{\Delta T}\right)^2} \tag{4.14}$$

It can be determined from equation 4.14 that the maximum uncertainty in the calculation of the Nusselt number is about 3.19%.

The comparison of experimental and analytical velocity profiles in a non-dimensional form is presented in figure 4.11(b). The experimental velocity profiles are plotted at different modified Grashof numbers corresponding to x = 50, 100, 140 mm and at a heat flux of 500 W/m^2. This figure shows a similarity in the experimental velocity profiles. The experimental inner and overall boundary layer thicknesses in non-dimensional form are calculated by taking the mean of all the values at different modified Grashof numbers (at x = 50, 75, 100, 125, 140 mm and heat fluxes of 500, 800, 1500 W/m^2). The mean value of inner and overall boundary layer thickness was measured to be 0.76 and 6.15 compared to analytical values of 0.71 and 6.58 respectively. This shows that the deviation in inner and overall boundary layer thickness from the analytical solution was 7.04% and 6.53% respectively.

Figure 4.11(c) shows the comparison of experimental and analytical local skin friction coefficient with the modified Grashof number. The analytical local skin friction coefficient is calculated from equation 4.7. For determining the experimental local skin friction coefficient, the velocity gradient at the wall is required, which is computed by curve fitting the data points in the inner layer of the velocity profile with an exponential equation of the form (Bejan, 2013) as,

$$u = A \times (1 - e^{-By}) \tag{4.15}$$

$$\left.\frac{\partial u}{\partial y}\right|_{y=0} = A \times B \tag{4.16}$$

where A and B are constants. The values of A and B depend on the modified Grashof number. A regression analysis of the data points results in a R-squared value of 0.99. In figure 4.11(c), the experimental local skin friction coefficients were evaluated at five different x = 50, 75, 100, 125 and 140 mm and at three different heat fluxes of 500, 800, 1500 W/m^2. It is observed from figure 4.11(c) that local skin friction coefficient decreases with the modified Grashof number. The analytical solution gives the value of the parameter $\frac{c_{fx}}{(Gr_x^*)^{-1/5}} = 0.2032$ for the $Pr = 6.14$. The experimental data gives the mean value of this parameter as 0.202 with a standard deviation of 0.012 which indicates that experimental and analytical skin friction coefficients are in close agreement.

(a)

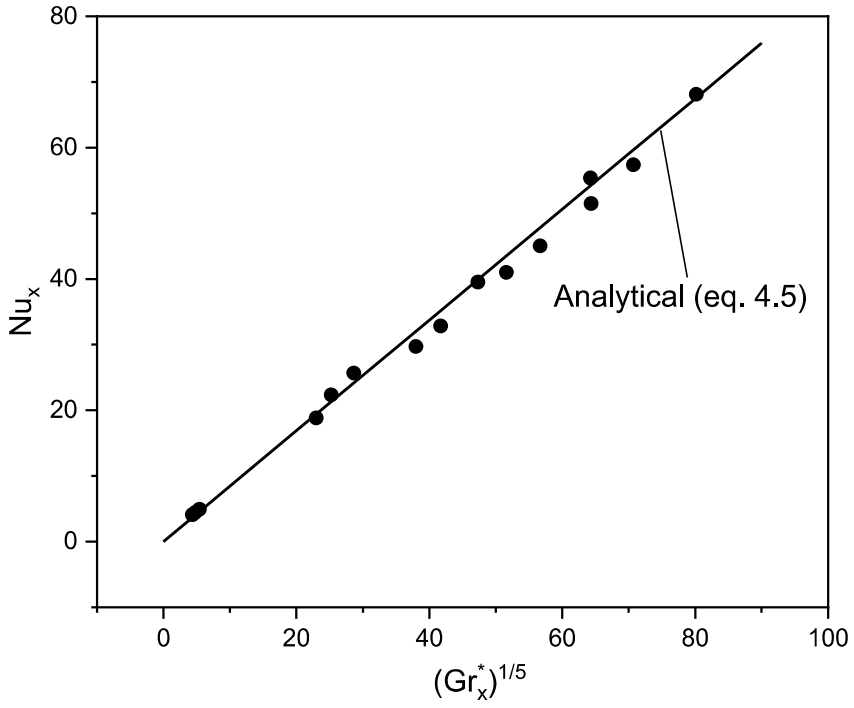

(b)

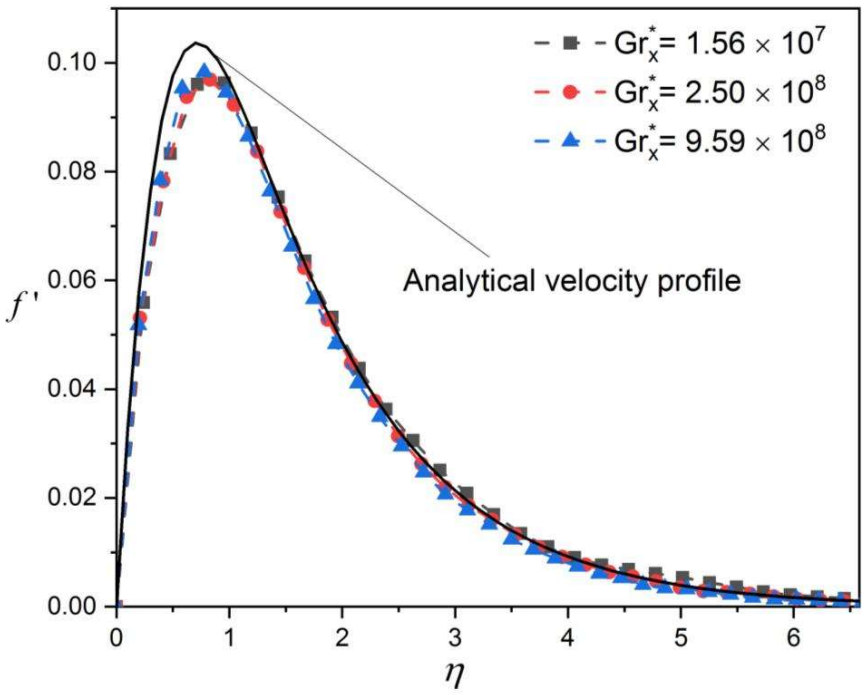

(c)

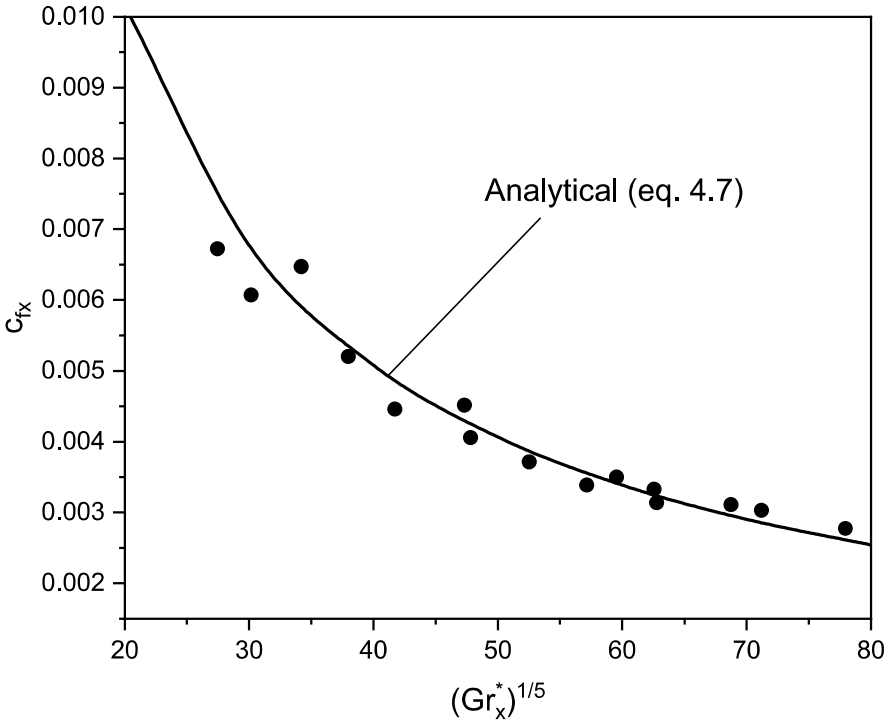

Figure 4.11: Comparison of experimental and analytical (a) local Nusselt number (b) velocity profile and (c) local skin friction coefficient at different modified Grashof numbers

4.3.5 Uncertainty analysis

There are two types of measurement errors: systematic and random [21]. The systematic error in PIV measurements is fixed and consists of magnification error, error in computation of particle displacement due to correlation algorithm and the bias in the camera timing [86,87]. The systematic error is less for a good calibration experiment [66]. Therefore, the main source of error is the random error and it has been estimated by repeating each experiment 3 times under identical conditions. The uncertainty calculated due to the random error in the velocity measurement with 95% confidence interval was estimated as

$$\epsilon_r = \frac{\pm 1.96\sigma}{V_i\sqrt{n}} \tag{4.17}$$

where $\sigma = \sqrt{\frac{\sum_{i=1}^{n}(V_i - \overline{V})}{n-1}}$ is the standard deviation, V_i is the velocity at a specific location for a particular experiment, $\overline{V}$ is the mean value of the velocity at a particular location for all experiments and n is the number of experiments performed with similar conditions. The value of ϵ_r was estimated as a maximum of ± 2.1% close to the wall.

4.4 Conclusion

In the present work, FCBL has been studied by PIV technique. The near wall measurements with this technique pose an experimental challenge due to factors such as a high velocity gradient, low seeding density and wall reflection. The effects of these factors have been reduced by painting the surface with matt black, employing background elimination technique, using suitably sized seeding particles and their concentration. Comparison of different methods for evaluation of particle displacement has been done. It was found that the ensemble correlation wherein wall is aligned with the interrogation area, gives better results close to the wall. Experiments were conducted at steady and laminar conditions with constant wall heat fluxes of 500, 800 and 1500 W/m^2. It was found that the

boundary layer consists of a thin inner layer (~ 2 mm) and a thicker outer layer (~ 15 mm). The results show that the thickness of the inner layer as well as overall boundary layer decreases with the heat flux and increases with the streamwise distance along the plate. The experimental results in a non-dimensional form, have been compared for the Nusselt number, velocity profile and skin friction coefficient with the analytical solution. It is found that the experimental and analytical results are in a broad agreement.